LAWRENCE
LIVERMORE
NATIONAL
LABORATORY

LLNL-JRNL-666719

# Exceptional Performance for Oxygen Reduction Reaction over Transition-Metal Doped PtNi Octahedra

X. Q. Huang, Z. P. Zhao, L. Cao, Y. Chen, E. Zhu, Z. Lin, M. Li, A. Yan, A. Zettl, Y. M. Wang, X. F. Duan, T. Mueller, Y. Huang

January 29, 2015

Science

## Disclaimer

# Exceptional Performance for Oxygen Reduction Reaction over Transition-Metal Doped PtNi Octahedra

Xiaoqing Huang,[1,2#] Zipeng Zhao,[1,2#] Liang Cao,[3] Yu Chen,[1,2] Enbo Zhu,[1,2] Zhaoyang Lin,[4] Mufan Li,[4] Aiming Yan,[5,6] Alex Zettl,[5,6,7] Y. Morris Wang,[8] Xiangfeng Duan,[2,4] Tim Mueller,[9*] and Yu Huang[1,2*]

[1]Department of Materials Science and Engineering, University of California, Los Angeles, California 90095, United States; [2]California NanoSystems Institute, University of California, Los Angeles, California 90095, United States; [3]Department of Physics and Astronomy, Johns Hopkins University, Baltimore, Maryland 21218, United States; [4]Department of Chemistry and Biochemistry, University of California, Los Angeles, California 90095, United States; [5]Department of Physics, and Center of Integrated Nanomechanical Systems, University of California, Berkeley, California 94720, United States, [6]Materials Sciences Division, Lawrence Berkeley National Laboratory, Berkeley, California 94720, United States; [7]Kavli Energy NanoSciences Institute at the University of California, Berkeley and the Lawrence Berkeley National Laboratory, Berkeley, California 94720, United States ; [8]Physical and Life Sciences Directorate, Lawrence Livermore National Laboratory, Livermore, California 94550, United States; [9]Department of Materials Science and Engineering, Johns Hopkins University, Baltimore, Maryland 21218, United States.

[#]These authors contributed equally.

*To whom correspondence should be addressed.

E-mails: tmueller@jhu.edu, yhuang@seas.ucla.edu,

**Bimetallic PtNi structures represent an emerging class of newly discovered electrocatalysts that are expected to exhibit exciting oxygen reduction reaction (ORR) activity. Despite considerable efforts, the limitations in terms of catalytic activity and durability have largely hindered the practical applications of PtNi nanocrystals. Here we report a surface engineering strategy based on the incorporation of various transition metal dopants onto the surface of dispersive PtNi/C octahedra (termed as M-PtNi/C, M=V, Cr, Mn, Fe, Co, Mo, W and Re). We demonstrate that these surface engineered PtNi catalysts exhibit impressive activity in the ORR, and their performance is highly dopant-dependent with Mo showing the best performance to date. Mo-PtNi/C shows simultaneously the highest specific activities of 10.3 $mA/cm^2$ to date and the unprecedented mass activity of 6.98 $A/mg_{Pt}$, approaching two orders of magnitude higher (81 and 73-fold enhancement in mass and specific activities, respectively) than that of the state-of-the-art commercial Pt/C catalyst (Alfa Aesar, 20 wt% Pt, 0.127 $mA/cm^2$ and 0.096 $A/mg_{Pt}$ ). Significantly the Mo-doped PtNi/C also exhibit outstanding durability showing negligible changes in the activity over the course of potential sweeps, in contrast to the obvious losses observed in its undoped PtNi/C counterpart. Theoretical calculations suggest Mo prefers subsurface positions near the particle edges in vacuum and surface vertex / edge sites in oxidizing conditions, and it plays important roles in enhancing both the performance and the stability of the PtNi catalyst. Our studies open up exciting**

**opportunities in catalyst design through fine tuning the chemical and electronic properties of the surface layer to achieve optimal performance which can impact broad catalytic applications including fuel cells, batteries and chemical production.**

Proton-exchange membrane (PEM) fuel cells are promising energy conversion devices for future transportation vehicles and portable electronic devices, due to their high energy density and specific energy, low environmental impact, and ability to operate at low temperatures *(1-5)*. A PEM fuel cell catalyzes reactions between the fuel (hydrogen, alcohols, etc.) at anode and the oxidant (molecular oxygen) at cathode, converting chemical energy of the fuel into electrical power *(6-8)*. Both the fuel reactions need catalysts to lower their electrochemical overpotential for high voltage output, and so far platinum (Pt) has been the universal choice of catalyst for both reactions *(9-11)*. To fully realize the commercial viability of fuel cells, especially for practical applications, the following challenges, which may not be strictly independent of one another, need to be simultaneously addressed: the high cost of Pt, the sluggish kinetics of the ORR and the low durability of the catalysts *(12-16)*.

A potential solution to address these challenges is alloying Pt with a secondary metal *(17-20)*. A Pt-based alloy with a lower content of scarce Pt metal can not only inherit the properties of the Pt constituent but also show improved performance when compared with pure Pt counterparts *(17-20)*. To this end, tremendous efforts have been invested in the pursuit of active and durable Pt-based electrocatalysts with a wide range of compositions *(21-25)*. PtNi nanostructures are predicted to exhibit superior activity for the ORR in bulk extended surfaces *(18)*, which has triggered extensive efforts in the development of PtNi nanoscale structures as

practical ORR catalysts *(26-30)*. However, although studies so far have led to considerable improvements in ORR performance, exceptional increases in activity as observed on bulk $Pt_3Ni(111)$ surface have not been realized yet *(26-30)*. Another major limitation of PtNi nanostructures is their low durability. The Ni element in these nanostructures leaches away gradually under detrimental corrosive ORR conditions, resulting in rapid performance losses *(28-32)*. Therefore, achieving Pt-based nanostructures with simultaneously high catalytic activity and durability remains an important open challenge *(33)*.

Here we demonstrate that by adopting a surface engineering strategy based on the control over dopant incorporation of various transition metals onto the surface of dispersive and octahedral PtNi/C (termed as M-PtNi/C, M=V, Cr, Mn, Fe, Co, Mo, W and Re), a new class of surface doped PtNi alloy catalysts are achieved which can exhibit an combination of high activity and stability. We specifically focused our efforts on $Pt_3Ni$-based nanocatalysts because the bulk extended $Pt_3Ni(111)$ surface has been shown to be one of the most efficient catalytic surface for the ORR. We show that the resulting surface-doped PtNi catalysts exhibit impressive activity in the ORR, and their performance is highly dopant-dependent. Especially, the newly generated Mo-PtNi/C for the first time simultaneously satisfies the overall criteria of high specific activity of 10.3 $mA/cm^2$, high mass activity of 6.98 $A/mg_{Pt}$, and significantly improved stability.

Fig. 1A shows a schematic of the experimental design and illustrates the fabrication procedure for our catalysts. In the first step, we prepared highly dispersive PtNi octahedra on commercial carbon black by an efficient one-pot approach without using any bulky capping

agents (Fig. S1). The transmission electron microscopy (TEM) and high-angle annular dark-field scanning TEM (HAADF-STEM) images of the obtained octahedral PtNi/C catalyst are shown in Fig. 1B-C, S2. It was clearly revealed that highly dispersive nanocrystals were grown on the carbon black. Those nanocrystals are nearly octahedral in shape and substantially uniform in size, averaging 4.2±0.2 nm in edge length. The Powder X-ray diffraction (PXRD) pattern of the colloidal products displays typical peaks located between those for Pt and Ni, which can be indexed as those of face-centered cubic (fcc) $Pt_3Ni$ (Fig. S3) *(34-35)*. The Pt/Ni composition was 74/26, as confirmed by inductively coupled plasma atomic emission spectroscopy (ICP-AES) and TEM energy-dispersive X-ray spectroscopy (TEM-EDS) (Fig. S4, Table S1). A HRTEM image taken from an individual octahedron indicates that it is a single crystal with well-defined fringes (Fig. 1D). The lattice spacing along the edge of the octahedron is 0.22 nm, consistent with the (111) lattice spacing of the fcc $Pt_3Ni$, confirming that the PtNi octahedra are bounded by the (111) planes. Fig. 1H shows the compositional line scanning profiles across an octahedron obtained by HAADF-STEM-EDS, where Pt and Ni elements were both distributed throughout the nanocrystal.

The surface doping for the PtNi/C catalyst was initiated by adding dopant precursors molybdenum hexacarbonyl ($[Mo(CO)_6]$) together with platinum(II) acetylacetonate ($[Pt(acac)_2]$) and nickel(II) acetylacetonate ($[Ni(acac)_2]$) into a suspension of PtNi/C in DMF and subsequently heating the reaction mixture at 170°C for 48 hours. Fig. 1E-F, show the TEM and STEM images of the product derived from the surface doping of PtNi/C by Mo (Mo-PtNi/C). We can see that dispersive Mo-PtNi/C nanocrystals with octahedral shape were obtained. The overall morphology of the doped Mo-PtNi/C catalyst was nearly the same as that of the original PtNi/C

catalyst. The lattice spacing along the edge of a Mo-PtNi/C shown in the HRTEM image is 0.22 nm (Fig. 1G), close to that of the plane of $Pt_3Ni$ alloy (0.22 nm). Both the compositional line profiles and X-ray photoelectron spectroscopy (XPS) show the presence of Pt, Ni and Mo in the catalyst (Fig. 1I, 1J). The Ni 2p and Pt 4f XPS spectra of Mo doped PtNi/C catalyst show that the majority of the surface Ni was in the oxidized state and the surface Pt was mainly in the metallic state, which are also observed by several recent PtNi-based studies *(33)*. Mo exhibits mainly Mo(6+) and Mo(4+) state. Similar phenomenon was observed in previous study, which showed Mo largely present in the form of $MoO_x$ on surface in PtMo alloy nanoparticles *(36)*. The overall molar ratio between Pt, Ni and Mo is 73.4:25.0:1.6, as indicated by inductively coupled plasma atomic emission spectroscopy (ICP-AES) result.

We further demonstrate that the surface doping approach is robust and can be readily extended to other metals, such as V, Cr, Mn, Fe, Co, et als by replacing molybdenum hexacarbonyl ($[Mo(CO)_6]$) with other corresponding transition-metal carbonyl in the above described process. In all transition-metal doped PtNi/C catalysts, highly dispersive nanocrystals with octahedral morphology anchored on carbon black were obtained (Fig. S5). The structures and compositions of all the transition-metal doped PtNi/C catalysts were confirmed by XPS and ICP-AES, confirming similar structure and surface compositions, as shown in Fig. S6 and Table S1. The successful fabrication of various transition-metal doped PtNi/C catalysts with well-defined size, morphology and surface composition readily enables us to compare the doping effects for PtNi/C made by various transition metals (Fig. 2).

To assess their catalytic activity towards the ORR, our catalysts were first loaded (with the same mass loading of Pt) onto glassy carbon electrodes. Cyclic voltammetry (CV) was used to evaluate the electrochemically active surface area (ECSA) of these catalysts. The ECSA can provide important information regarding the number of available active sites, with a higher ECSA indicating that more available electrochemical active sites. Commercial Pt/C catalyst (20 wt% Pt on Vulcan XC72R carbon, Pt particle size: 2-5 nm) obtained from Sigma-Aldrich was used as a baseline catalyst for comparison (Fig. S7). Fig. 2A compares the CV curves on these different catalysts recorded in $N_2$-purged perchloric acid solution at a sweep rate of 100 mV/s. The current responses from hydrogen adsorption/desorption processes appear in the potential range of 0.05-0.35 V. The ECSA was calculated by measuring the charge collected in the hydrogen adsorption/desorption region after double-layer correction and assuming a value of 210 $\mu C/cm^2$ for the adsorption of a hydrogen monolayer. The octaheral PtNi/C and Mo-PtNi/C catalysts display similar and high ECSA of 66.6 $m^2/g$ and 67.5 $m^2/g$, respectively, which is comparable to that of the commercial Pt/C (75.6 $m^2/g$, Pt particle size: 2-5 nm) catalyst.

The ORR measurements were performed in $O_2$-saturated 0.1 M $HClO_4$ solutions by using a glassy carbon rotating disk electrode (RDE) at room temperature with a sweep rate of 10 mV/s. Fig. 2B shows the ORR polarization curves for the different catalysts, which were normalized by the area of the glassy carbon area (0.196 $cm^2$). The polarization curves display two distinguishable potential regions: the diffusion-limiting current region below 0.6 V and the mixed kinetic-diffusion control region between 0.6 and 1.1 V. We calculated the kinetic currents from the ORR polarization curves by considering the mass-transport correction *(37)*. In order to compare the activity for different catalysts, the kinetic currents were normalized with

respect to both ECSA and the loading amount of metal Pt. As shown in Fig. 2C, the octahedral Mo-PtNi/C exhibits a specific activity of 10.3 mA/cm$^2$ at 0.9 V versus a reversible hydrogen electrode (RHE), which represents the highest specific activity ever achieved in ORR catalysts. In contrast, the specific activity of undoped PtNi/C catalyst is about 2.7 mA/cm$^2$. Based on the mass loading of Pt, the mass activity of Mo-PtNi/C catalyst was calculated to be 6.98 A/mg$_{Pt}$, also the best value achieved in Pt-based ORR catalysts to date. **The specific activity of Mo-PtNi/C catalyst exhibits an impressive improvement factor of 81 over commercial Pt/C catalyst, while the mass activity of the Mo-PtNi/C catalyst achieves an unprecedented 73-fold enhancement. No matter calculated at 0.90 V and/or 0.95 V, both the specific and mass activities of the Mo-PtNi/C based on $H_{upd}$ and/or CO stripping methods (Fig. S8) are much higher than those of the state-of-art PtNi catalysts *(26, 29)* and even better than those of the recently reported PtNi nanoframes catalyst *(33)*, making the Mo-PtNi/C catalysts among the most active electrocatalyst achieved in ORR catalysts reported to date (Table S2).**

As Mo-doped PtNi/C (Mo-PtNi/C) exhibits an exceptional activity towards ORR, we further examined the doping effects for PtNi/C modified by other transition metals. Seven other PtNi/C catalysts doped with V, Cr, Mn, Fe, Co, W, and Re were made (termed as V-PtNi/C, Cr-PtNi/C, Mn-PtNi/C, Fe-PtNi/C, Co-PtNi/C, W-PtNi/C and Re-PtNi/C, respectively) and used as the catalysts for the ORR under the same test conditions. Fig. 2C summarizes the electrochemical properties of the various doped PtNi/C catalysts (See Fig. S9 for individual sample measurement). The ECSAs of undoped PtNi/C, V-PtNi/C, Cr-PtNi/C, Mn-PtNi/C, Fe-PtNi/C, Co-PtNi/C, Mo-PtNi/C, Re-PtNi/C and W-PtNi/C catalysts are 66.6, 65.1, 67.8, 65.3, 66.4, 67.8, 67.5, 66.4, and 68.8 m$^2$/g (Fig. 2C, top panel), respectively, which are all comparable to that of the

state-of-the-art commercial Pt/C (75.6 $m^2$/g, Pt particle size: 2-5 nm) catalyst, indicating the excellent surface exposure of all the surface doped PtNi/C catalysts. All the doped PtNi/C catalysts show effective catalytic behavior towards the ORR but with highly distinct activities. The activities of the doped PtNi/C catalysts are strongly dependent on the dopants used. None of the other dopants resulted in a catalyst with activity as high as the Mo-doped catalyst (Fig. 2C, middle panel). The change of mass activities in various doped PtNi/C catalysts is also very similar to that of the specific activities (Fig. 2C, bottom panel). Remarkably, the Mo-PtNi/C catalyst showed the best catalytic activity with the highest specific activity and the highest mass activity to date. Considering that all the doped PtNi/C catalysts have similar ECSA and all the doped PtNi/C catalysts are derived from the same PtNi/C catalysts, the observation of the exceptional catalytic activity in Mo-PtNi/C catalyst is particularly significant, which strongly demonstrates the pronounced impact of the transition metal dopants on the ORR activity of the PtNi octahedra.

The above results demonstrate that the Mo-PtNi/C catalyst exhibits the highest ORR activity in terms of both specific and mass activities to date. We further evaluated the electrochemical durability of the octahedral Mo-PtNi/C catalyst by using an accelerated durability test (ADT) between 0.6 and 1.1 V (vs RHE) in $O_2$-saturated 0.1 M $HClO_4$ at a scan rate of 50 mV/s. The undoped octahedral PtNi/C catalyst was used as a baseline catalyst for comparison. After 4000 and 8000 potential cycles, the variations in both the ECSA and electrocatalytic activity of the ORR were determined. We observed that the Mo-PtNi/C catalyst largely retained its ECSA and activity (Fig. 3A). The octahedral Mo-PtNi/C catalyst exhibited only 1- and 3-mV shift for its half-wave potential after 4000 and 8000 potential cycles, respectively.

After 8000 cycles, the CV measurement showed a small change in ECSA for the octahedral Mo-PtNi/C catalyst. In contrast, the undoped PtNi/C catalyst was unstable under the same reaction conditions, and its polarization curves showed 33-mV negative shifts after durability tests (Fig. 3B). After 8000 cycles, the activity of the Mo-PtNi/C catalyst was still as high as 9.7 $mA/cm^2$ and 6.6 $A/mg_{Pt}$ (Fig. 3C), which is 76-fold (~93.8% of the initial value) and 69-fold (94.5% of the initial value) higher than those of the commercial Pt/C catalyst, respectively. However, for the undoped PtNi/C catalyst, only 33% and 41% of the initial specific activity and mass activity were preserved after 8000 cycles (Fig. 3C). After the durability tests the electrocatalysts were further examined by TEM. As shown in Fig. S4, while the size of the PtNi/C catalyst was largely maintained, their morphologies became rounder. The change of the morphology likely results from the Ni loss after potential cycles, as confirmed by EDX and XPS analyses (Fig. S4, S10, the Pt/Ni composition ratio changes from 74.3/25.7 to 88.1/11.9); in contrast, the corresponding morphology and composition changes for Mo-PtNi/C catalyst were negligible (The Pt/Ni/Mo ratio changes from 73.4/25.0/1.6 to 74.5/24.0/1.5), suggesting that durability of the Mo-PtNi/C is dramatically improved compared with those of the undoped octahedral PtNi/C catalyst.

To investigate the cause of the enhanced durability of the Mo-PtNi/C catalysts, cluster expansions of Pt-Ni-Mo nanoparticles were used in Monte Carlo simulations *(38-40)* to identify low-energy nanoparticle and (111) surface structures for computational analysis (Details are provided in the supplemental information). These structures include predicted ground states for a nanoparticle with composition $Mo_6Ni_{41}Pt_{178}$ (Fig. S11), a 9-layer slab with composition $Mo_2Ni_7Pt_{27}$ (Fig. S12), and nanoparticles with size, shape, and compositions matching those of the experimentally observed nanoparticles (Figs. 4, S13). In vacuum, the equilibrium particle

structures predicted by the cluster expansion have a Pt skin, with Mo atoms preferring sites in second atomic layer along the edges connecting two different (111) facets (Fig. 4). Density functional theory (DFT) *(41)* calculations revealed that the subsurface site is preferable to the lowest-energy neighboring surface site by 1.110 eV per Mo atom on the $Mo_6Ni_{41}Pt_{178}$ nanoparticle and by 0.881 eV per Mo atom on the $Mo_2Ni_7Pt_{27}$ extended (111) surface. In the presence of adsorbed oxygen on the (111) surface (with ¼ monolayer coverage), the situation reverses: there is a driving force of 1.559 eV per Mo atom for Mo to segregate to the surface, and the oxygen preferentially adsorbs atop the surface Mo atom. Similar results were found for the $Mo_6Ni_{41}Pt_{178}$ nanoparticle, where oxygen was found to strongly drive Mo segregation to the surface. This suggests the formation of surface Mo-oxide species, consistent with our XPS measurements. Our calculations on the $Mo_6Ni_{41}Pt_{178}$ particle indicate that oxidized Mo preferentially segregates to a vertex site, where the adsorbed oxygen is predicted to be stable against reduction to $H_2O$ down to a potential of -0.1 V vs. the RHE. Our computational prediction that Mo favors sites near the particle edges and vertices is consistent with the dopant distributions shown in our STEM-EELS (electron energy loss spectroscopy) line scan results (Fig.S14).

Our calculations suggest possible explanations for the enhanced stability of the Mo-PtNi/C particles. We predict that doping the nanoparticles with Mo directly stabilizes both Ni and Pt atoms against dissolution and may inhibit diffusion through the formation of relatively strong Mo-Pt and Mo-Ni bonds. The cluster expansion was used to evaluate the effects of substituting a single Mo atom into all the sites in a representative 4.2 nm $Ni_{831}Pt_{2366}$ particle (Fig. S13). The presence of a neighboring Mo atom increases the energy required to remove a Pt atom from a

surface site by between 163 and 486 meV (depending on the local atomic structure), and it increases the energy required to remove a Ni atom from a surface site by between 85 and 335 meV, which are proved experimentally (Fig.S15). If the Mo atom is on an edge or vertex site, the energy required to remove a Pt (Ni) atom from a neighboring edge or vertex site increases by 346 (170) to 450 (214) meV. These values are consistent with DFT calculations on the $Mo_6Ni_{41}Pt_{178}$ nanoparticle which predict that the presence of a Mo atom on a vertex site stabilizes the Pt atom on the neighboring vertex site by 458 (444) meV with (without) an oxygen atom adsorbed atop the Mo atom. The evidence that Mo may have a particularly stabilizing effect on undercoordinated sites suggests that Mo atoms may also pin step edges on the surface, inhibiting the dissolution process.

Due to the relatively strong Mo-Pt and Ni-Pt nearest-neighbor bonds, both Mo and Ni prefer to occupy similar sites with many Pt nearest neighbors. However in oxidizing conditions the energetic driving force for Mo segregation to the surface is much stronger than the driving force for Ni segregation. For the $Mo_2Ni_7Pt_{27}$ slab with ¼ monolayer oxygen coverage, the calculated driving force for $2^{nd}$-layer Mo to migrate to the surface is 1.559 eV per atom, as opposed to 0.284 eV per atom for Ni. This suggests that in oxidizing conditions Mo atoms may "crowd out" Ni atoms on the particle surface, reducing the number of surface Ni atoms available for dissolution. These results are consistent with our experimental data that, while PtNi/C suffers great Ni loss during ORR cycling, the Ni content in Mo-PtNi/C stays nearly constant (Fig.S10).

Although the exact mechanisms by which the surface doped $Pt_3Ni$ shows exceptional catalytic performance demand more detailed studies, we suggest that the presence of transition-metal dopants near the surface of doped PtNi/C catalysts alters the surface electronic properties of Pt as manifested in the negative 0.16 eV shift of Pt 4f 7/2 peaks in XPS spectra (Fig. S6I). The XPS spectra are supported by our DFT calculations, in which the surface d-band center is decreased by 0.14 eV in the $Mo_2Ni_7Pt_{27}$ slab and by 0.06 eV in the 1.9 nm $Mo_6Ni_{41}Pt_{178}$ nanoparticle relative to the comparable $Ni_9Pt_{27}$ slab and $Ni_{47}Pt_{178}$ nanoparticle. We calculated the oxygen binding energy, an indicator of the binding energies of other oxygenated species *(43)*, for all fcc and hcp sites on the (111) facets of both the $Mo_6Ni_{41}Pt_{178}$ and $Ni_{47}Pt_{178}$ nanoparticles. The average oxygen binding energy is lowered by 44 meV in the $Mo_6Ni_{41}Pt_{178}$ nanoparticle, in agreement with the lower surface d-band center *(42)*. However the binding energy varies significantly among different sites, with the strongest bonds found near the particle edges and the weakest found nearest the center of the (111) facets (Fig. 5a). The difference in oxygen binding energies between the two particles also varies significantly across the surface (Fig. 5b). Compared to the $Ni_{47}Pt_{178}$ nanoparticle, the oxygen binding energies in the $Mo_6Ni_{41}Pt_{178}$ particle near the Mo atoms are decreased by up to 154 meV, and binding energies at sites closer to the center of the (111) facet are *increased* by up to 102 meV.

The local changes in oxygen binding energies provide a possible explanation for the some of the observed increase in specific activity in PtNi/C upon Mo doping. A Sabatier volcano of ORR catalysts predicts that ORR activity will be maximized when the oxygen binding energy is about 0.2 eV less than the binding energy on Pt(111) *(44)*. Our calculations predict that sites near the particle edge bind oxygenated species too strongly, as in Pt(111), and sites near the

facets of the particles bind oxygenated species too weakly, as in $Pt_3Ni(111)$ (Fig. 5a). If Mo migrates to the thermodynamically favored sites near the particle edges, it will decrease the oxygen binding energies at nearby adsorption sites, moving these sites closer to the peak of the volcano plot and increasing their catalytic activity. Similarly, our calculations suggest it may increase the oxygen binding energies at sites closer to the center of the (111) facet that bind oxygen too weakly. As a result of these shifts, some sites near the Mo dopant may have oxygen binding energies close to the peak of the volcano plot, making them highly active for catalysis. Together, our studies demonstrate that by engineering the surface structure of the octahedral PtNi nanocrystal, it is possible to fine tune the chemical and electronic properties of the surface layer and hence modulate its catalytic activity.

In summary, we have presented a surface doping strategy based on the control over dopant incorporation of transition-metals on the surface of dispersive PtNi octahedra, which can enable a new design of Pt-based ORR electrocatalysts with impressive specific activities and mass activities, to satisfy critical requirements for highly efficient electrocatalytic applications. With the use of Mo as the dopant, the newly generated Mo-PtNi/C catalyst can deliver unprecedented activities that are approaching two orders of magnitude higher than those of the state-of-the-art commercial Pt/C catalyst, which represents the highest activities ever achieved in the Pt-based ORR catalysts to date. Significantly, the Mo-PtNi/C catalyst showed negligible decay in activity over the course of 8000 cycles, in contrast to obvious losses observed with its undoped PtNi/C counterpart under the same conditions. Thus, our finding opens up exciting opportunities towards the rational design of practically relevant catalysts

with enhanced activity and durability, which can significantly impact broad areas such as batteries, fuel cells, fine chemical production and beyond.

**References**


1. F. T. Bacon, *Nature* **186**, 589 (1960).

2. M. S. Dresselhaus, I. L. Thomas, *Nature* **414**, 332 (2001).

3. M. Winter, R. J. Brodd, *Chem. Rev.* **104**, 4245 (2004).

4. Y. J. Wang, D. P. Wilkinson, J. J. Zhang, *Chem. Rev.* **111**, 7625 (2011).

5. M. K. Debe, *Nature* **486**, 43 (2012).

6. Y. H. Bing, H. S. Liu, L. Zhang, D. Ghosh, J. J. Zhang, *Chem. Soc. Rev.* **39**, 2184 (2010).

7. D. S. Su, G. Q. Sun, *Angew. Chem., Int. Ed.* **50**, 11570 (2011).

8. Z. W. Chen, D. Higgins, A. P. Yu, L. Zhang, J. J. Zhang, *Energ. Environ. Sci.* **4**, 3167 (2011).

9. J. Y. Chen, B. Lim, E. P. Lee, Y. N. Xia, *Nano Today* **4**, 81 (2009).

10. J. B. Wu, H. Yang, *Acc. Chem. Res.* **46**, 1848 (2013).

11. N. S. Porter, H. Wu, Z. W. Quan, J. Y. Fang, *Acc. Chem. Res.* **46**, 1867 (2013).

12. H. A. Gasteiger, S. S. Kocha, B. Sompalli, F. T. Wagner, *Appl. Catal. B: Environ.* **56**, 9 (2005).

13. F. A. de Bruijn, V. A. T. Dam, G. J. M. Janssen, *Fuel Cells* **8**, 3 (2008).

14. J. Greeley, I. E. L. Stephens, A. S. Bondarenko, T. P. Johansson, H. A. Hansen, T. F. Jaramillo, J. Rossmeisl, I. Chorkendorff, J. K. Norskov, *Nat. Chem.* **1**, 552 (2009).

15. H. A. Gasteiger, N. M. Markovic, *Science* **324**, 48 (2009).

16. J. K. Nørskov, T. Bligaard, J. Rossmeisl, C. H. Christensen, *Nat. Chem.* **1**, 37 (2009)

17. V. R. Stamenkovic, B. S. Mun, M. Arenz, K. J. J. Mayrhofer, C. A. Lucas, G. F. Wang, P. N. Ross, N. M. Markovic, *Nat. Mater.* **6**, 241 (2007).

18. V. R.Stamenkovic, B. Fowler, B. S. Mun, G. F. Wang, P. N. Ross, C. A. Lucas, N. M. Markovic, *Science* **315**, 493 (2007).

19. A. S. Arico, P. Bruce, B. Scrosati, J. M. Tarascon, W. Van Schalkwijk, *Nat. Mater.* **4**, 366 (2005)

20. S. J. Guo, S. Zhang, S. H. Sun, *Angew. Chem., Int. Ed.* **52**, 8526 (2013).

21. J. B. Wu, A. Gross, H. Yang, *Nano. Lett.* **11**, 798 (2011).

22. J. Zhang, J. Y. Fang, *J. Am. Chem. Soc.* **131**, 18543 (2009).

23. Y. J. Kang, C. B. Murray, *J. Am. Chem. Soc.* **132**, 7568 (2010).

24. Y. E. Wu, S. F. Cai, D. S. Wang, W. He, Y. D. Li, *J. Am. Chem. Soc.* **134**, 8975 (2012).

25. D. L. Wang, H. L. L. Xin, R. Hovden, H. S. Wang, Y. C. Yu, D. A. Muller, F. J. DiSalvo, H. D. Abruna, *Nat. Mater.* **12**, 81 (2013).

26. S. I. Choi, S. F. Xie, M. H. Shao, J. H. Odell, N. Lu, H. C. Peng, L. Protsailo, S. Guerrero, J. H. Park, X. H. Xia, J. G. Wang, M. J. Kim, Y. N. Xia, *Nano. Lett.* **13**, 3420 (2013).

27. J. Zhang, H. Z. Yang, J. Y. Fang, S. Z. Zou, *Nano. Lett.* **10**, 638 (2010).

28. X. Q. Huang, E. B. Zhu, Y. Chen, Y. J. Li, C. Y. Chiu, Y. X. Xu, Z. Y. Lin, X. F. Duan, Y. Huang, *Adv. Mater.* **25**, 2974 (2013).

29. C. H. Cui, L. Gan, M. Heggen, S. Rudi, P. Strasser, *Nat. Mater.* **12**, 765 (2013).

30. M. K. Carpenter, T. E. Moylan, R. S. Kukreja, M. H. Atwan, M. M. Tessema, *J. Am. Chem. Soc.* **134**, 8535 (2012).

31. J. Snyder, I. McCue, K. Livi, J. Erlebacher, *J. Am. Chem. Soc.* **134**, 8633 (2012).

32. H. Y. Zhu, S. Zhang, S. J. Guo, D. Su, S. H. Sun, *J. Am. Chem. Soc.* **135**, 7130 (2013).

33. C. Chen, Y. J. Kang, Z. Y. Huo, Z. W. Zhu, W. Y. Huang, H. L. Xin, J. D. Snyder, D. G. Li, J. A. Herron, M. Mavrikakis, M. F. Chi, K. L. More, Y. D. Li, N. M. Markovic, G. A. Somorjai, P. D. Yang, V. R. Stamenkovic, *Science* **343**, 1339 (2014).

34. K. Ahrenstorf, O. Albrecht, H. Heller, A. Kornowski, D. Gorlitz, H. Weller, *Small* **3**, 271 (2007).

35. Y. E. Wu, D. S. Wang, Z. Q. Niu, P. C. Chen, G. Zhou, Y. D. Li, *Angew. Chem., Int. Ed.* **51**, 12524 (2012).

36. Z. Liu, J. E. Hu, Q. Wang, K. Gaskell, A. I. Frenkel, G. S. Jackson, B. Eichhorn, *J. Am. Chem. Soc.* **131**, 6924. (2009).

37. B. Lim, M. J. Jiang, P. H. C. Camargo, E. C. Cho, J. Tao, X. M. Lu, Y. M. Zhu, Y. N. Xia, *Scienc*e **324**, 1302 (2009).

38. J. M. Sanchez, F. Ducastelle, D. Gratias, *Physica* **128A**, 334 (1984).

39. N. Metropolis, A. Rosembluth, M. Rosembluth, A. Teller, *J. Chem. Phy.* **21**, 1087 (1953).

40. T. Mueller, G. Ceder, *Phy. Rev. B* **80**, 024103 (2009).

41. W. Kohn, L. J. Sham, *Phys. Rev.* **140**, A1133 (1965).

42. B. Hammer, J. K. Nørskov, in *Advances in Catalysis,* H. K. Bruce C. Gates, Ed. (Academic Press, 2000), vol. Volume 45, pp. 71-129.43. J. Rossmeisl, A. Logadottir, J. K. Nørskov, *Chem. Phys.* **319**, 178 (2005).

44. J. Rossmeisl, G. S. Karlberg, T. Jaramillo, J. K. Norskov, *Faraday Discussions* **140**, 337 (2009).

45. K. Momma, F. Izumi, *J. Appl. Crystallogr.* **41**, 653 (2008).

**Acknowledgement**

We acknowledge the support from ARO through Award No. 54709-MS-PCS and the ONR under Award N00014-08-1-0985. Computational studies were supported by the NSF through award DMR-1352373 and using computational resources provided by XSEDE through awards DMR130056 and DMR140068. Atomic-scale structural images were generated using VESTA *(45)*. We thank the Director, Office of Energy Research, Office of Basic Energy Sciences, Materials Sciences and Engineering Division, of the US Department of Energy under Contract No. DE-AC02-05CH11231, under the $sp^2$-bonded materials program, for TEM analytical measurements performed at the National Center for Electron Microscopy at the Lawrence Berkeley National Laboratory. The work at LLNL was performed under the auspices of the US Department of Energy under contract No. DE-AC52-07NA27344. A.Y. and A.Z. received additional support from NSF grant EEC-083219 within the Center of Integrated Nanomechanical Systems. We also thank Electron Imaging Center of Nanomachines at CNSI for the TEM support. Y.H. acknowledges the support from Sloan Research Fellowship.

**Author contributions**

Y.H. and X.D. conceived and supervised the research. Y.H., X.D., X.H. and Z.Z. designed the experiments. X.H. and Z.Z. performed most of the experiments and data analysis. X.H., Z. Z., Y.C., E. Z., Z.L., M.L., A. Y. and Y. W. participated in various aspects of the experiments and discussions. L.C. and T.M. designed and performed the computational modeling. Y.H., X. D., T.M.

and X.H. co-wrote the paper. All authors discussed the results and commented on the manuscript.

**Additional information**

Supplementary Information is linked to the online version of this paper at http://www.sciencemag.org/.

**Competing financial interests**

The authors declare no competing financial interests.



Correspondence and requests for materials should be addressed to Y.H. (yhuang@seas.ucla.edu) or T.M. (tmueller@jhu.edu).

## Figures

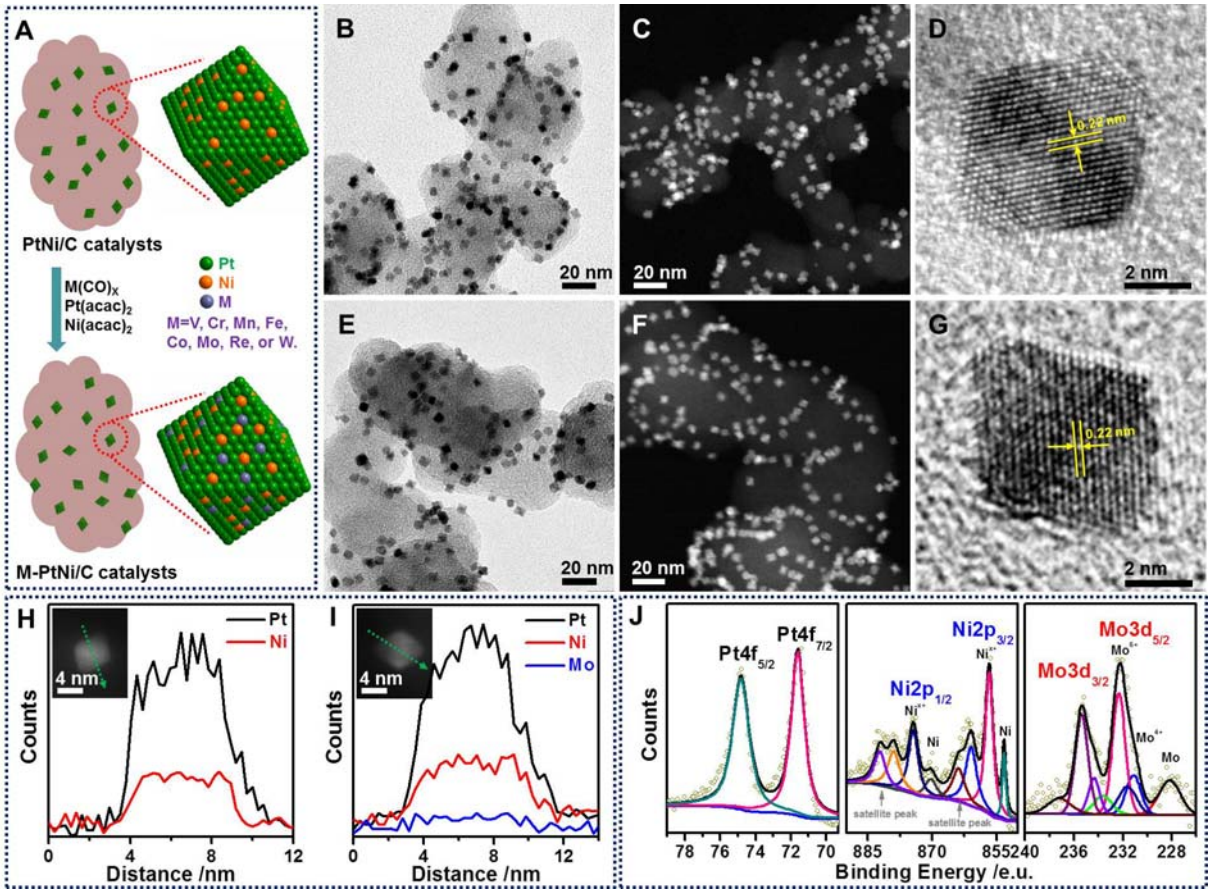


**Fig. 1I Schematic illustration of the fabrication process and the structure analyses for the transition-metal doped PtNi/C catalysts.** (A) A schematic illustration of the fabrication of various well-defined octahedral transition-metal doped PtNi/C catalysts. (B) Representative low-magnification TEM and (C) HAADF-STEM images of the octahedral PtNi/C catalysst. (D) HRTEM image on an individual octahedral PtNi/C nanocrystal. (H) Line-scanning profile across an octahedral PtNi/C nanocrystal, which is indicated in the inset of (H). (E) Representative low-magnification TEM and (F) HAADF-STEM images of the octahedral Mo-PtNi/C catalyst. (G) HRTEM image on an individual octahedral Mo-PtNi/C nanocrystal. (I) Line-scanning profile across an octahedral Mo-PtNi/C nanocrystal, which is indicated in the inset of (I). (J) Pt, Ni and Mo XPS spectra for the octahedral Mo-PtNi/C catalyst.

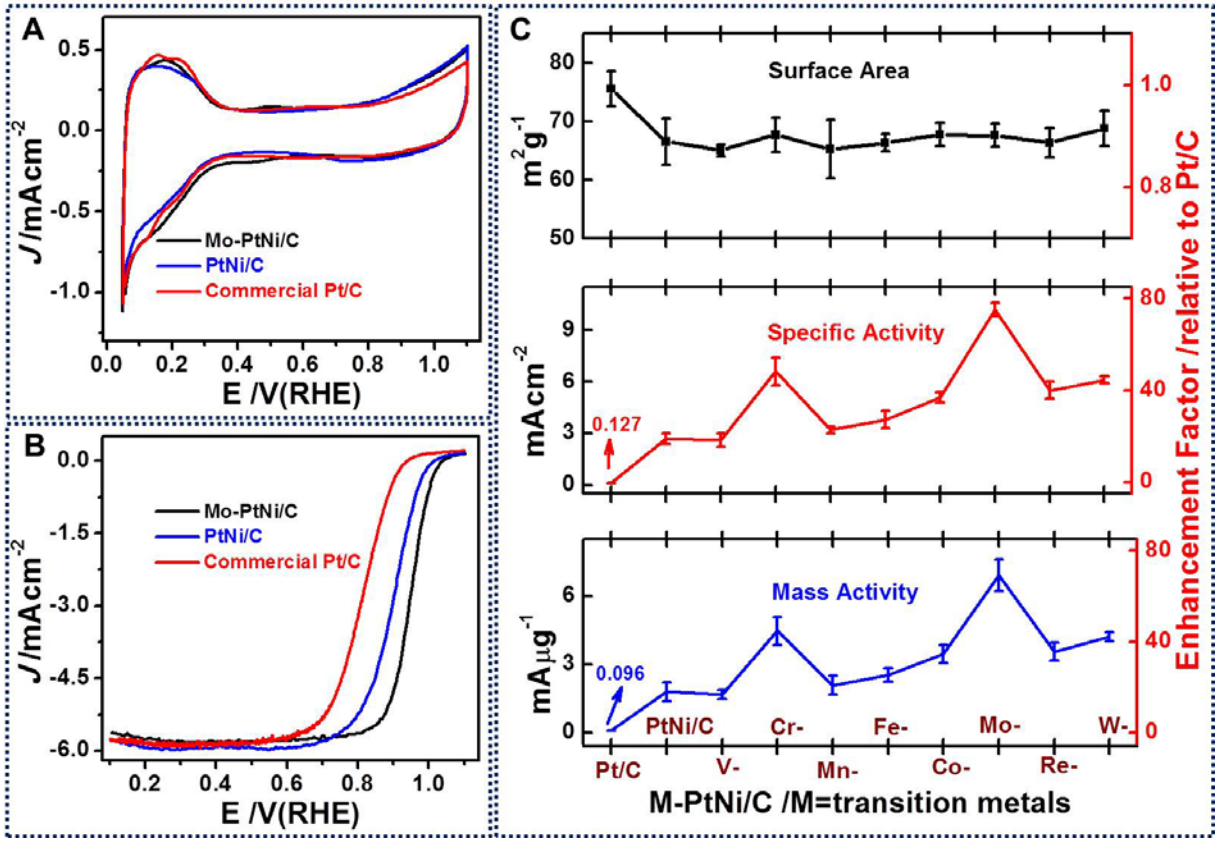


**Fig. 2I Electrocatalytic properties of high-performance transition-metal doped octahedral PtNi/C catalysts and commercial Pt/C catalyst.** (A) Cyclic voltammograms of octahedral Mo-PtNi/C, octahedral PtNi/C and commercial Pt/C catalysts recorded at room temperature in $N_2$-purged 0.1 M $HClO_4$ solution with a sweep rate of 100 mV/s. (B) ORR polarization curves of octahedral Mo-PtNi/C, octahedral PtNi/C and commercial Pt/C catalysts recorded at room temperature in an $O_2$-saturated 0.1 M $HClO_4$ aqueous solution with a sweep rate of 10 mV/s and a rotation rate of 1600 rpm. (C) The electrochemically active surface area (ECSA, up panel), specific activity (middle panel) and mass activity (bottom panel) at 0.9 V versus RHE for these transition-metal doped PtNi/C catalysts, which are given as kinetic current densities normalized to the ECSA and the loading amount of Pt, respectively. In (A) and (B), current densities were normalized in reference to the geometric area of the RDE (0.196 $cm^2$).

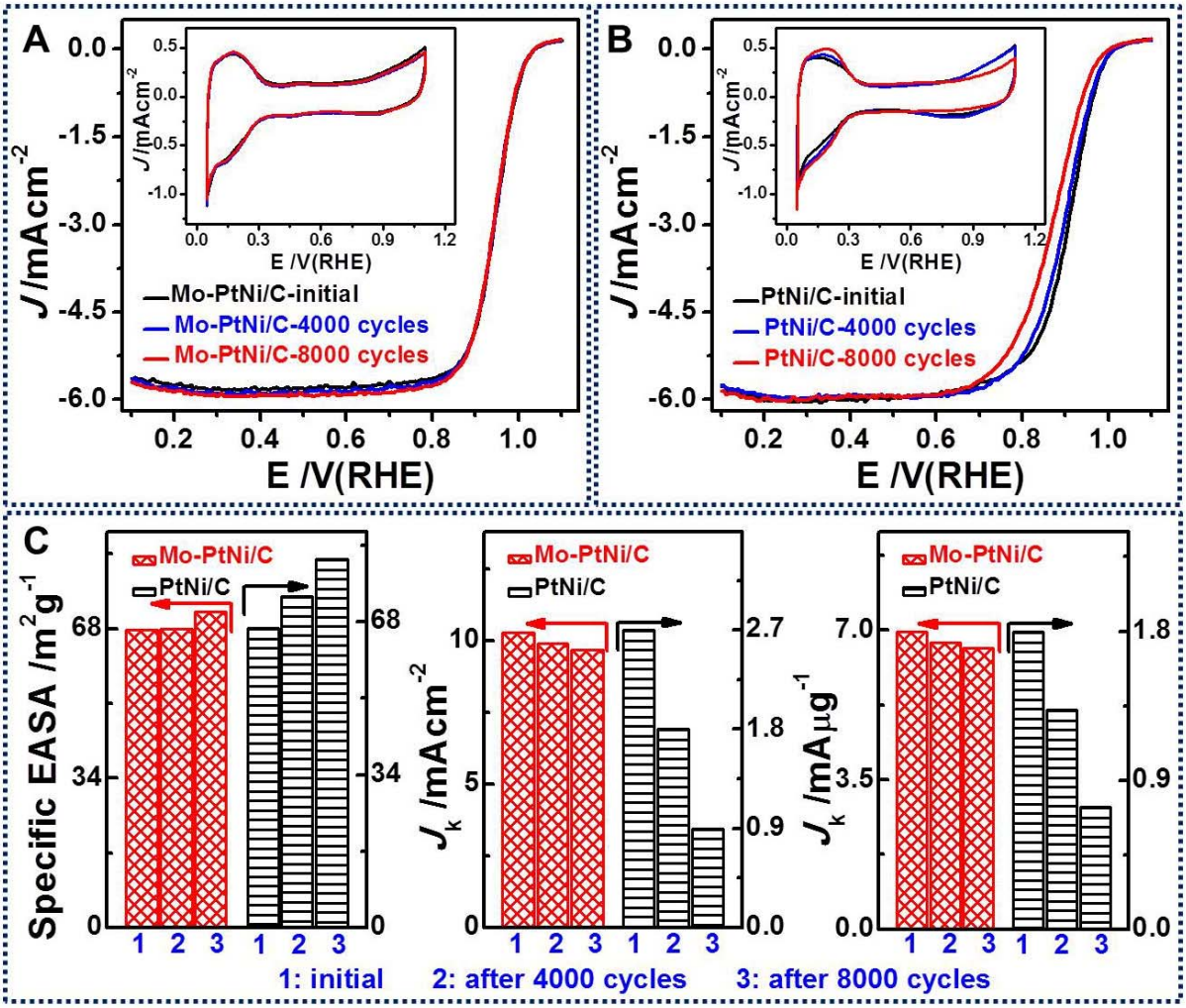


**Fig. 3I Electrochemical durability of the high-performance octahedral Mo-PtNiCo/C catalyst and octahedral PtNi/C catalyst.** ORR Polarization curves and (inset) corresponding cyclic voltammograms of (A) the octahedral Mo-PtNi/C catalyst and (B) the octahedral PtNi/C catalyst before, after 4000 and after 8000 potential cycles between 0.6-1.1 V vs. RHE. (C) The changes of ECSAs (left panel), specific activities (middle panel) and mass activities (right panel) of octahedral Mo-PtNi/C catalyst and octahedral PtNi/C catalyst before, after 4000 and after 8000 potential cycles. The durability tests were carried out at room temperature in $O_2$-saturated 0.1 M $HClO_4$ at a scan rate of 50 mV/s.

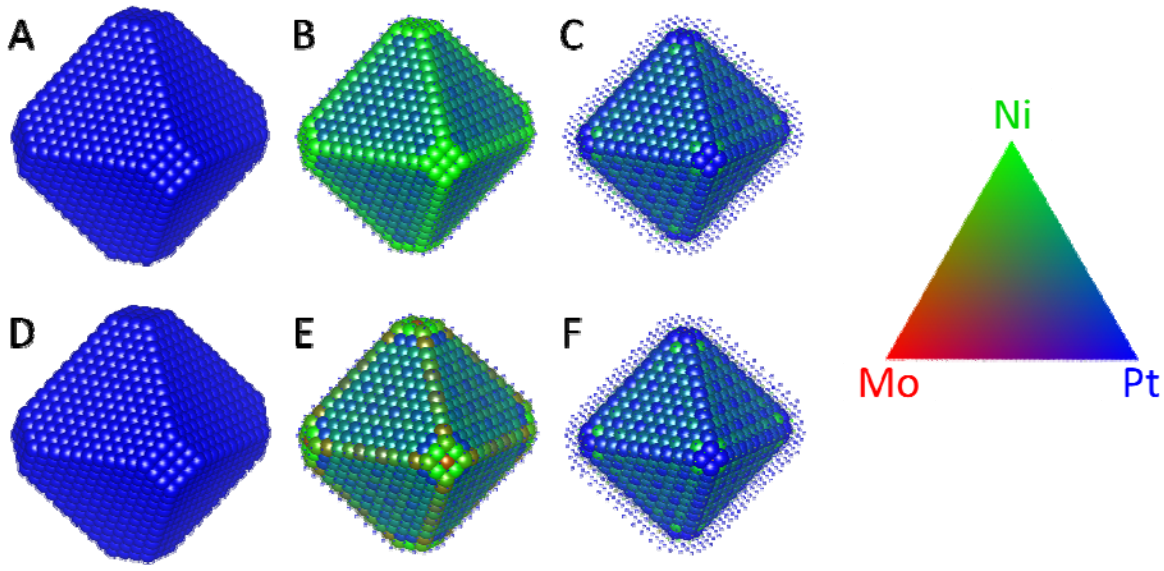


**Fig. 4I The average site occupancies of the (A) first, (B) second, and (C) third layers in the $Ni_{831}Pt_{2366}$ nanoparticle and the (D) first, (E) second, and (F) third layers in the $Mo_{51}Ni_{799}Pt_{2347}$ nanoparticle at 170°C as determined by a Monte Carlo simulation.** Blue spheres represent pure Pt, green represent pure Ni, and red represent pure Mo. Other colors represent fractional occupancies, as indicated by the color triangle on the right. Small spheres represent the positions of atoms in the outer layers.

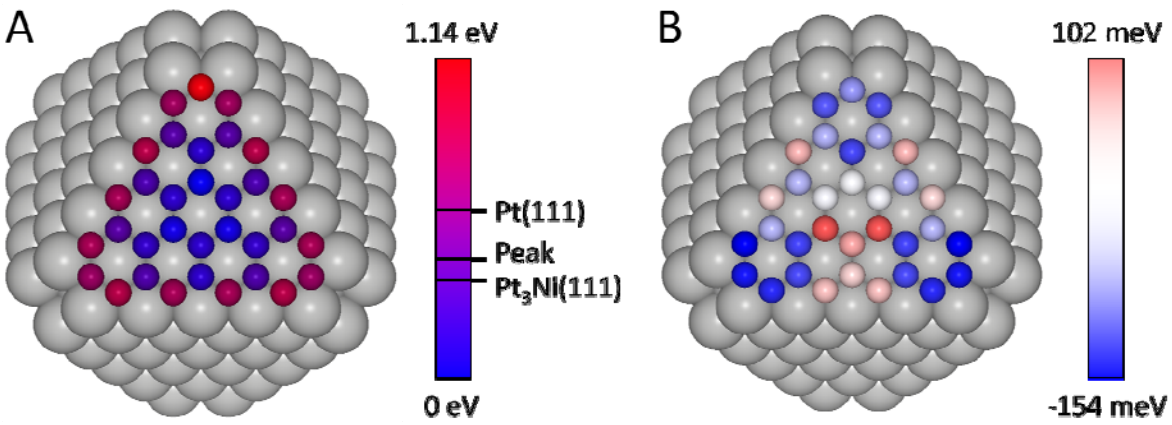


**Fig. 5I Oxygen binding energies on the predicted ground state $Mo_6Ni_{41}Pt_{178}$ nanoparticle. (**A) The calculated binding energies for a single oxygen atom on all fcc and hcp sites on the (111) facet, relative to the lowest binding energy. Grey spheres represent Pt and colored spheres represent oxygen sites. Three binding energies are provided for reference: the calculated binding energy on the fcc site of a pure Pt (111) surface, the binding energy corresponding to the peak of the Sabatier volcano, and the binding energy on a $Pt_3Ni(111)$ surface *(44)*. (B) The change in binding energies when a $Ni_{47}Pt_{178}$ nanoparticle is transformed to a $Mo_6Ni_{41}Pt_{178}$ nanoparticle by the substitution of Mo on its energetically favored sites in the second layer below the vertices.